

# Effect of Off-Body Laser Discharge on Drag Reduction of Hemisphere Cylinder in Supersonic Flow-Part II

Nadia Kianvashrad\* and Doyle Knight†

*Rutgers - The State University of New Jersey, New Brunswick, New Jersey 08903, USA*

Stephen P. Wilkinson,‡ Amanda Chou,‡ George B. Beeler,‡ and Moazzam Jangda§

*NASA Langley Research Center, Hampton, VA, 23681, USA*

**The interaction of on-axis and off-axis laser discharge in front of a hemisphere cylinder in Mach 2.0 flow is investigated numerically. Details of the physics of the interaction of the laser-induced shock and the heated region with the bow shock and its effect on drag reduction are included. The energetic efficiency of the laser discharge in reducing drag is calculated.**

## I. Introduction

Drag reduction as a result of energy deposition in supersonic flow has been demonstrated in several experimental and numerical studies. Artem'ev et al.<sup>1</sup> showed a drag reduction up to 80% for a blunt cylinder using a thin heated filament. Tretyakov et al.<sup>2</sup> reported up to 45% drag reduction for conical and hemispherical objects by means of high frequency laser discharge. Riggins et al.<sup>3</sup> showed 30% to 50% drag reduction for blunt bodies in hypersonic flows using a laser discharge. Lashkov et al.<sup>4</sup> reported centerline pressure reduction for a blunt cylinder and a hemisphere by means of a microwave discharge. Adelgren et al.<sup>5</sup> showed a 40% centerline pressure reduction for a hemisphere using a laser discharge. Knight et al.<sup>6</sup> reported a centerline pressure reduction for a hemisphere by means of a microwave discharge. Schülein et al.<sup>7</sup> reported a centerline pressure reduction for a hemisphere due to single and double laser discharges. Kim et al.<sup>8</sup> showed a 21% drag reduction and up to 500% energetic efficiency for a right circular cylinder using a repetitive laser discharge. Kremeyer et al.<sup>9</sup> reported up to 96% drag reduction and up to 6500% energetic efficiency using a line source. Knight<sup>10</sup> presents a review of computational and experimental drag reduction studies.

From the literature, as cited above, there is a wide range of results for both drag reduction and energetic efficiency. The objective of this paper is to understand the efficiency of energy deposition for a single laser discharge upstream of a hemisphere cylinder at Mach 2. We perform a sensitivity analysis of the gas dynamic energetic efficiency (defined as the ratio of the energy saved due to drag reduction to the actual energy absorbed by the gas) to the discharge parameters. Both on- and off-axis discharges are considered.

## II. Description of Experiments

A hemisphere-cylinder, blunt-body wind tunnel test is currently being planned<sup>11</sup> at Mach 2 in the NASA Langley 20-inch Supersonic Wind Tunnel.<sup>12</sup> The model is a 50.8 mm diameter hemisphere cylinder, which is illustrated in Fig. 1. The planned experimental measurements are 1) the actual energy absorbed by the gas, 2) impulse on the hemisphere cylinder due to laser discharge versus time, and 3) energetic efficiency.

---

\*PhD Candidate, Department of Mechanical and Aerospace Engineering, AIAA Student Member. Email: nadiakianvashrad@gmail.com

†Professor, Department of Mechanical and Aerospace Engineering, AIAA Member. Email: doyleknight@gmx.com

‡Research Aerospace Engineer, Flow Physics & Control Branch, AIAA Senior Member.

§Research Aerospace Engineer, Flow Physics & Control Branch

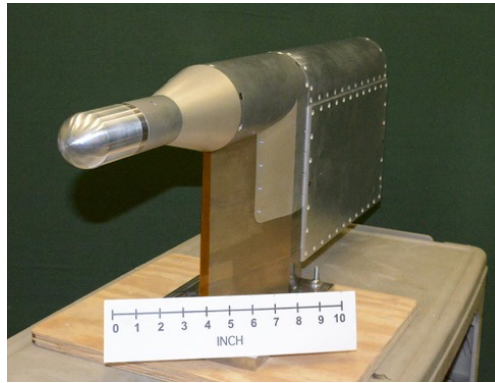


**Figure 1. Hemisphere cylinder model.**

### III. Description of Computations

The governing equations are the nonequilibrium compressible laminar Navier-Stokes equation with Park I thermochemistry model<sup>13</sup> and the Landau-Teller translational-rotational energy exchange.<sup>14</sup> The complete description of the governing equations are presented in Kianvashrad and Knight.<sup>15</sup> The governing equations are solved using a C++ code written by the authors with the implementation of Message Passing Interface (MPI). The code is a finite volume method with the Roe flux scheme<sup>16</sup> and Monotone Upstream Scheme for Conservation Laws (MUSCL) reconstruction<sup>17</sup> based on the primitive variables. The central difference method is used for calculation of viscous fluxes. A Data Parallel Line Relaxation (DPLR) method<sup>18</sup> is used for marching in time to achieve a high CFL (Courant-Friedrichs-Lewy) number. The calculations are performed using a 48-core Linux cluster.

The schematic of the axisymmetric computational domain for the laser discharge calculation in front of the hemisphere cylinder is shown in Fig. 2. The boundary conditions are: streamwise axis from point A to B, isothermal no-slip wall from B to D, outflow zero gradient from D to E, and fixed boundary condition from E to F and F to A. The computational domain consists of 2.16 M cells and has uniform spacing along the surface and normal to the wall. Table 1 presents the grid properties of the calculations.

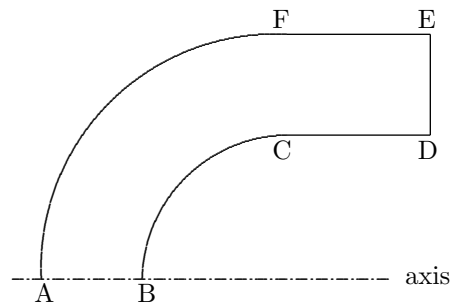


**Figure 2. Computational domain.**

In the planned experiments, the laser discharge will be focused on the axis of symmetry. However, it is possible that the laser may not discharge exactly on the axis of symmetry. To consider this possibility in the calculation, a three-dimensional computation around the hemisphere cylinder was performed for an off axis laser discharge. Figure 3 shows the schematic of the computational domain for this case. Due to the existence of a plane of symmetry, only half of the hemisphere cylinder is considered. The computational domain consists of 6.84 M cells and has uniform spacing along the surface and normal to the wall. Table 2 presents the grid properties of the three-dimensional calculation.

**Table 1. Computational grid (2.16 M cells).**

$il$	$jl$	$kl$	$\Delta\xi$ ( $\mu\text{m}$ )	$\Delta\eta$ ( $\mu\text{m}$ )	$\Delta\phi$ (in degree)
600	600	6	133.00	84.67	2

LEGEND

$il$	No. of cells along surface
$jl$	No. of cells away from surface
$kl$	No. of cells in azimuthal direction
$\xi$	Direction along surface
$\eta$	Direction away from surface
$\phi$	Azimuthal cell angle

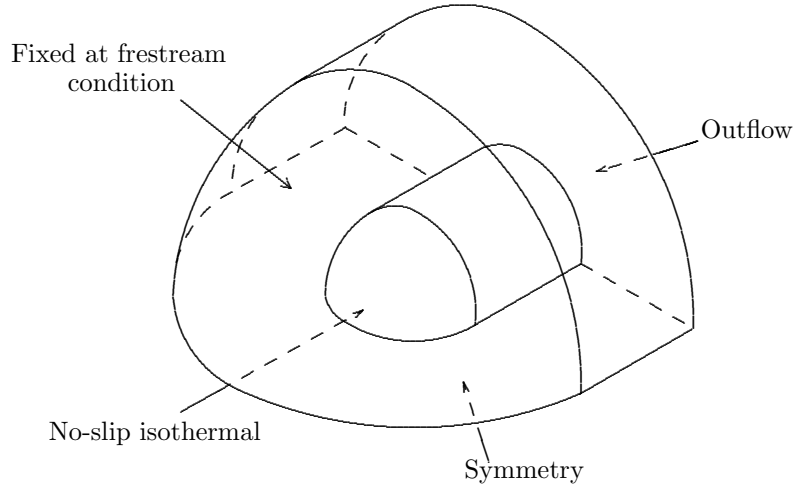


**Figure 3. Computational domain for three-dimensional calculation.**

**Table 2. Computational grid for three-dimensional calculation (6.84 M cells).**

$il$	$jl$	$kl$	$\Delta\xi$ ( $\mu\text{m}$ )	$\Delta\eta$ ( $\mu\text{m}$ )	$\Delta\phi$ (in degree)
192	198	180	264.58	38.49	1

LEGEND

$il$	No. of cells along surface from hemisphere tip to the end of cylinder
$jl$	No. of cells away from surface
$kl$	No. of cells in azimuthal direction
$\xi$	Direction along surface
$\eta$	Direction away from surface
$\phi$	Azimuthal cell angle

## IV. Results

This section is divided into two parts: 1) on-axis laser discharge with the axisymmetric computational domain and 2) off-axis laser discharge with the three-dimensional computational domain.

## A. On-Axis Laser Discharge

Four computations are performed with the freestream condition of Table 3 and the actual energies absorbed by the gas due to laser discharge of 12.5 mJ, 25 mJ, 50 mJ, and 100 mJ. The Reynolds number,  $Re_\infty$ , is based on the hemisphere radius  $R$ . The hemisphere cylinder surface is considered as an isothermal wall with  $T_w = 294.48$  K. The laser discharge is modeled as an instantaneous heating of a spherical region upstream of the hemisphere cylinder. It is assumed that the energy absorbed by the gas increases both translational-rotational and vibrational temperatures to the same value. These temperatures along with the location of discharge and the initial radius of discharge are presented in Table 4. The flow is from left to right and this direction is considered as the  $x$ -direction. The initial flow condition is the converged solution of the hemisphere cylinder in the flow with the same freestream conditions as given in Table 3.

**Table 3. Freestream conditions.**

Variables	Freestream condition
$M_\infty$	2.0
$T_\infty$	172.74 K
$P_\infty$	17.635 kPa
$\rho_\infty$	0.354 kg/m <sup>3</sup>
$Y_{N_2}$	0.765
$Y_{O_2}$	0.235
$Re_\infty$	406280
$T_w$	294.48 K

**Table 4. Heated region initial conditions.**

Absorbed Energy	12.5 mJ	25 mJ	50 mJ	100 mJ
$T^{\text{vib}} = T$	833 K	1342 K	2234 K	3880 K
Radius of discharge	2.54 mm	2.54 mm	2.54 mm	2.54 mm
Discharge location upstream	0.84R	0.84R	0.84R	0.84R
Density	$\rho_\infty$	$\rho_\infty$	$\rho_\infty$	$\rho_\infty$

To understand the physics of interaction, the case with 100 mJ energy absorbed by the gas is used for explanation. Figs. 4 and 5, respectively, display contour plots of Mach number (top section of each figure) and vibrational temperature of species  $N_2$  (bottom section of each figure), and contour plots of density gradient magnitude (top section of each figure) and dimensionless pressure, i.e., pressure divided by freestream pressure (bottom section of each figure) at specified times where the instantaneous laser discharge corresponds to  $t = 0$  s (Figs. 4(a) and 5(a)). At  $t = 48.17 \mu\text{s}$  (Figs. 4(b) and 5(b)), the interaction of the heated region with the bow shock has begun. As a result of this interaction, the heated region is compressed. The lower Mach number of the heated region moves the bow shock forward (upstream), which is known as the “lensing” phenomenon in the previous studies such as Adelgren et al.<sup>5</sup> and Schülein et al.<sup>7</sup> A  $\lambda$ -shock is formed at the interaction of the distorted part of the bow shock and the original bow shock, which was also reported by Schülein et al.<sup>7</sup> Two vortex rings are formed due to the Richtmyer-Meshkov instability. Figs. 4(c) and (d) and Figs. 5(c) and (d) demonstrate the slow movement of the vortices along the hemisphere surface. Furthermore, at  $t = 240.83 \mu\text{s}$ , the heated region has completely passed and the bow shock has returned to its original position (Figs. 4(d) and 5(d)).

Fig. 6 shows the change in the force (the total of pressure and viscous terms) on the hemisphere in the  $x$ -direction as a result of the laser discharge nondimensionalized by  $F_x^\circ$  (the force in  $x$ -direction before the laser is discharged) versus time for all four cases of energy added to the gas. The forces are calculated over the entire hemisphere cylinder. The lower horizontal axis is the dimensionless time,  $tU_\infty/R$ , where  $R$  is the hemisphere radius. The upper horizontal axis is dimensional time in  $\mu\text{s}$  where  $t = 0$  s is the instant that the

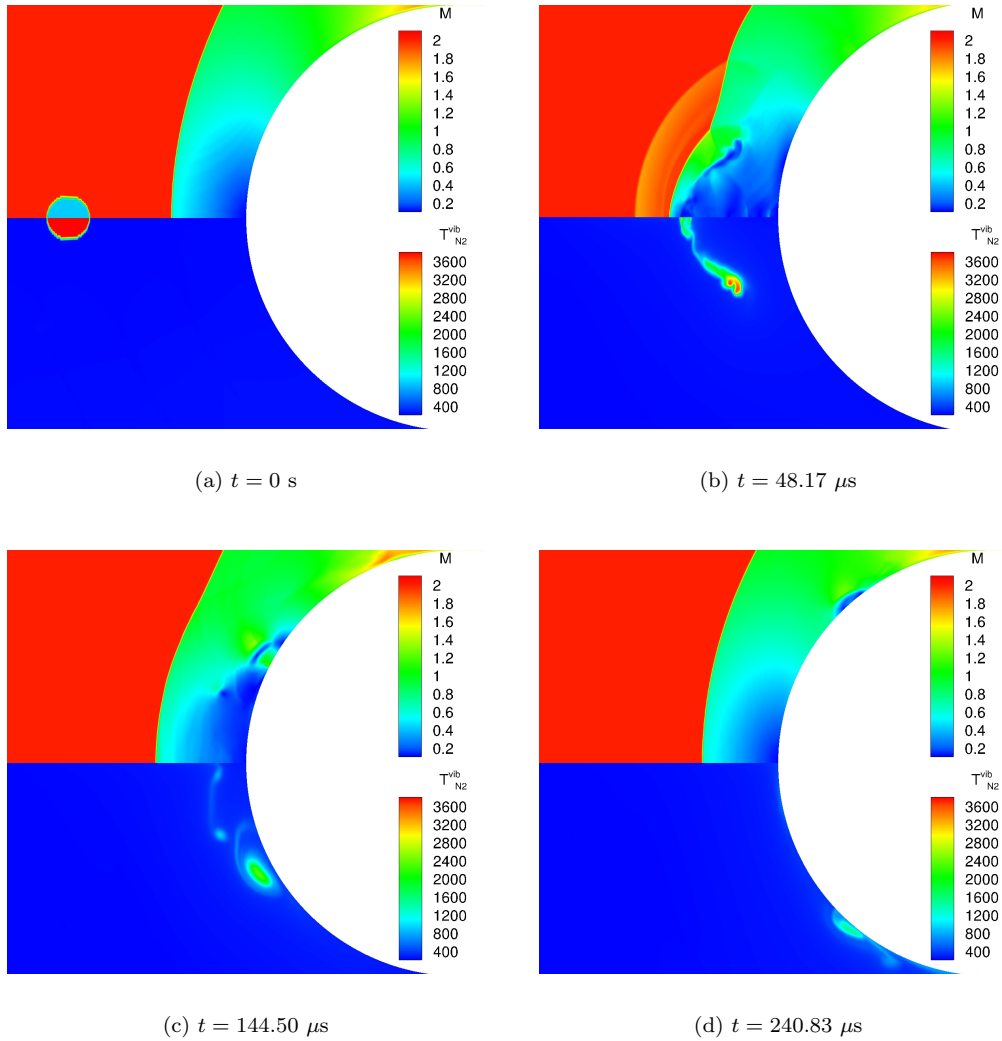


**Figure 4. Contour plots of Mach number and vibrational temperature of  $N_2$  for  $\Delta E = 100$  mJ.**

laser discharge is added to the flow. Dashed lines show the zero change in the force, i.e., total force equal to the total drag force of the hemisphere cylinder before laser discharge.

The first peak in the force change is due to the interaction of the shock wave with the hemisphere surface, which increases the pressure at the surface and hence the drag force. The expansion wave propagation due to the interaction of the heated region and bow shock reduces the pressure and generates the negative peak in force. The second compression wave creates the second peak. The creation of vortices and their slow movement around the hemisphere surface as displayed by Figs. 4(c) and 4(d) is the reason for the long lasting drag reduction, which extends for about four dimensionless times. The dimensionless time of one is the time the freestream flow requires to pass a distance equal to the hemisphere radius.

Comparison of the force change versus time for the four cases of 12.5 mJ, 25 mJ, 50 mJ, and 100 mJ shows that all the positive and negative peak values are increased with increasing energy absorbed by the gas, which is a result of the stronger interaction of the shock induced by the laser discharge and the bow shock, and the heated region and the bow shock. Additionally, the more significant drag reduction in the higher energy case is due to the stronger vortices, which are created as a result of the interaction of the heated region and the bow shock. The stronger the vortices, the lower the pressure at the vortex cores, which reduces the pressure force over the hemisphere cylinder.

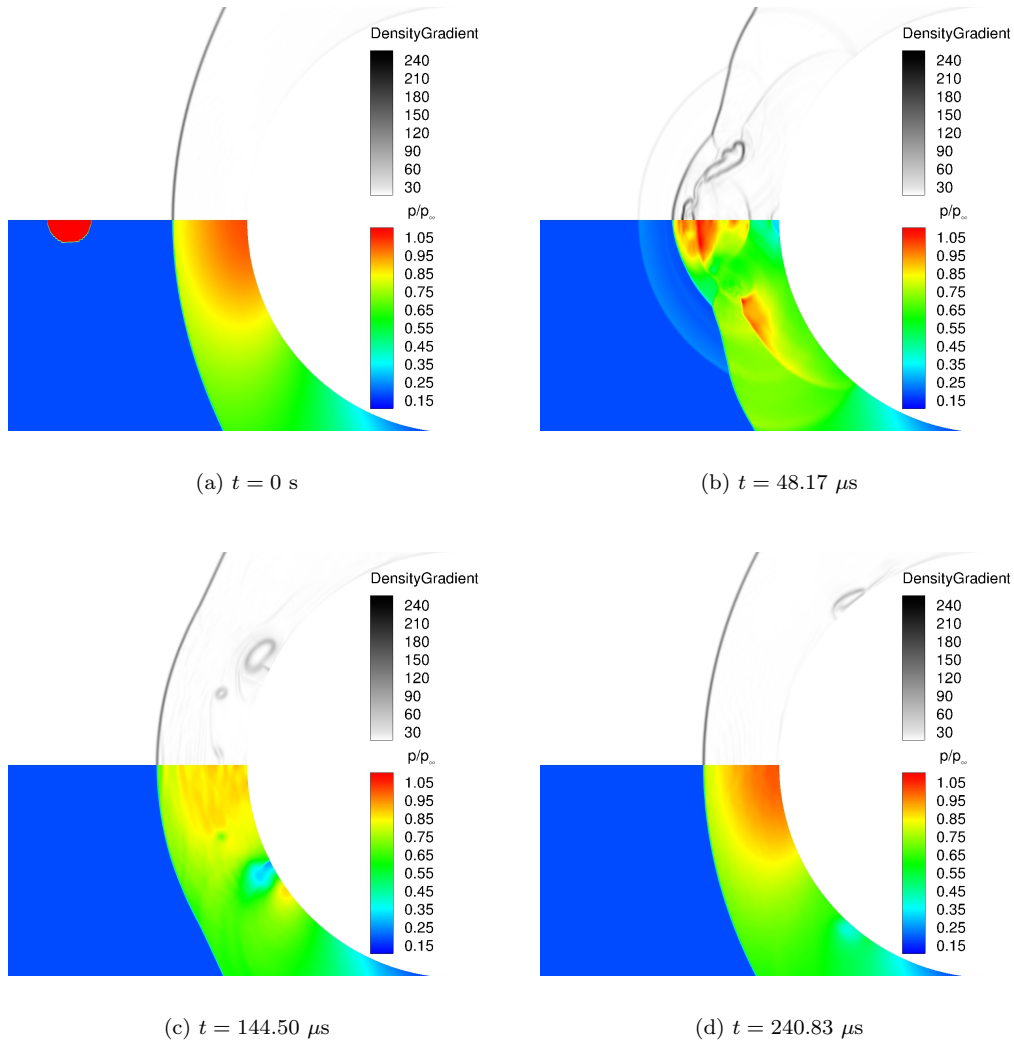


**Figure 5. Contour plots of density gradient and dimensionless pressure for  $\Delta E = 100$  mJ.**

The gas dynamic energetic efficiency is defined as the ratio of energy saved due to the interaction of the laser discharge to the energy absorbed by the gas. The energy saved is the negative of the change in the impulse times the inflow velocity. Thus, the gas dynamic energetic efficiency (GDEE) is calculated as

$$\text{GDEE} = -\frac{u_\infty \Delta \text{Impulse}}{\Delta E} \quad (1)$$

The change in the impulse due to laser discharge are calculated using Fig. 6. The gas dynamic energetic efficiencies of these simulations are presented in Table 5. The increase in the energy absorbed by the gas from 12.5 mJ to 25 mJ increased the gas dynamic energetic efficiency. However, increasing the energy absorbed by the gas from 25 mJ to 100 mJ has almost no effect on the energetic efficiency. It seems there is an asymptotic line for the gas dynamic energetic efficiency curve as a function of energy absorbed by the gas. The change in the impulse created as a result of laser discharge interaction with hemisphere cylinder is larger for higher energy absorbed by the gas, however, since the energy absorbed by the gas itself is higher, the gas dynamic energetic efficiency is almost constant for 25 mJ to 100 mJ energies absorbed by the gas.

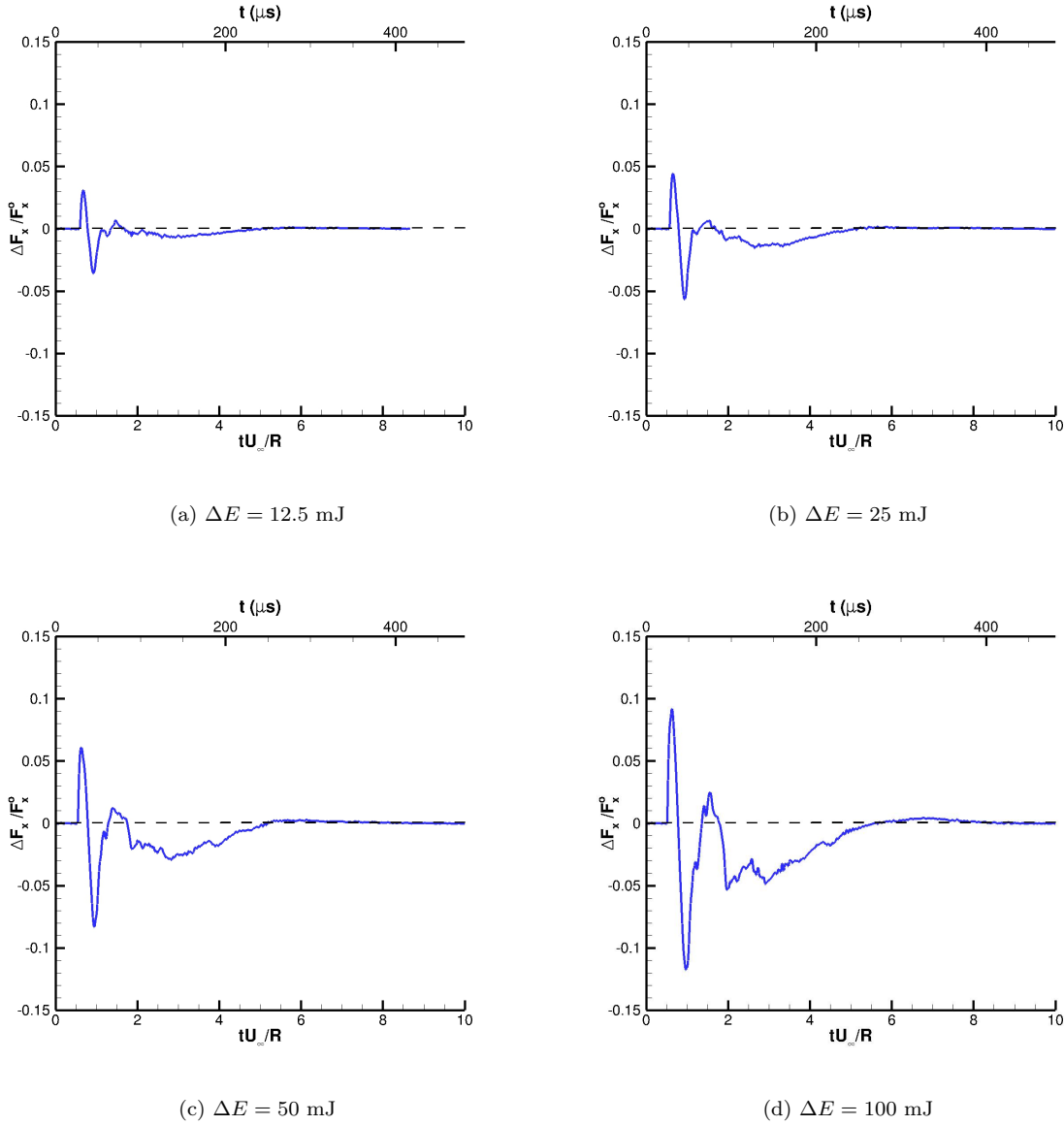


Figure 6. Dimensionless pressure force change versus time.

Table 5. Energetic efficiency for different energy absorbed by the gas

Absorbed energy	12.5 mJ	25 mJ	50 mJ	100 mJ
GDEE	2.3	3.0	3.0	2.9

## B. Off-Axis Laser Discharge

A computation is performed with the freestream condition of Table 6 and the actual energy absorbed by the gas due to laser discharge of 51 mJ. The Reynolds number,  $Re_\infty$ , is based on the hemisphere radius  $R$ , which is equal to 2.54 cm. The hemisphere cylinder surface is considered as an isothermal wall with  $T_w = 294.48$  K. The laser discharge is modeled as an instantaneous heating of a spherical region upstream of the hemisphere cylinder. It is assumed that the energy absorbed by the gas increases both translational-rotational and

vibrational temperatures to the same value. These temperatures along with the location of discharge and the initial radius of discharge are presented in Table 7. The flow is from left to right and this direction is considered as the  $x$ -direction. The initial flow condition is the converged solution of the hemisphere cylinder in the flow with the same freestream conditions as given in Table 6.

**Table 6. Freestream conditions.**

Variables	Freestream condition
$M_\infty$	2.0
$T_\infty$	172.74 K
$P_\infty$	17.635 kPa
$\rho_\infty$	0.354 kg/m <sup>3</sup>
$Y_{N_2}$	0.765
$Y_{O_2}$	0.235
$Re_\infty$	406022
$T_w$	294.48 K

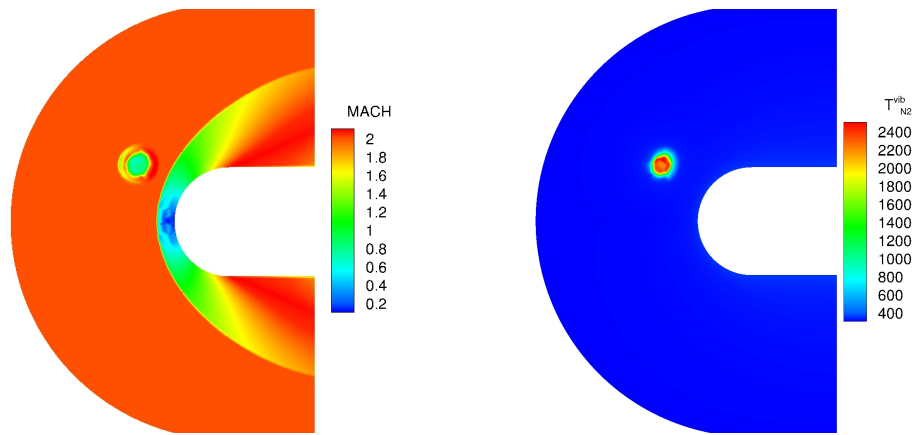
**Table 7. Heated region initial conditions.**

Absorbed Energy	51 mJ
$T^{\text{vib}} = T$	2238 K
Radius of discharge	2.54 mm
Discharge location above axis	1.0499 $R$
Discharge location upstream of hemisphere tip	0.9643 $R$
Density	$\rho_\infty$

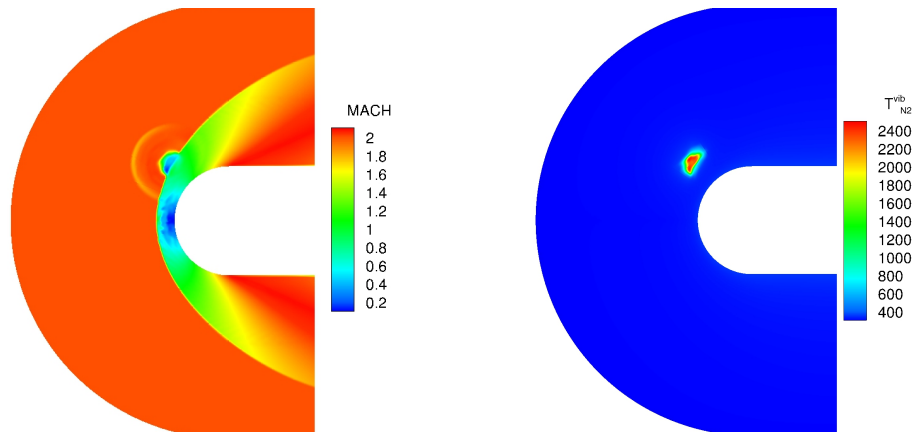
Fig. 7 displays contour plots of Mach number (on the left side) and the vibrational temperature of species  $N_2$  (on the right side) at specified times where the instantaneous laser discharge corresponds to  $t = 0$  s. At  $t = 14.45 \mu\text{s}$  (Fig. 7(a)), the blast wave is visible close to the heated region. At  $t = 43.35 \mu\text{s}$  (Fig. 7(b)), the interaction of the heated region with the bow shock has begun. As a result of this interaction, the heated region is compressed. The lower Mach number inside the heated region is where the ‘‘lensing’’ phenomenon is observed. Due to the Richtmyer-Meshkov instability, a vortex is formed that moves along the hemisphere cylinder. This vortex is more easily visualized using the vibrational temperature. The vibrational temperatures of each diatomic species inside the vortex are reduced in time. Moreover, at  $t = 120.41 \mu\text{s}$ , the heated region has completely passed the bow shock and the bow shock has returned to its original position (Fig. 7(c)).

Fig. 8 shows the change in the total force (the total of pressure and viscous terms) on the hemisphere in the  $x$  and  $y$ -directions as a result of the laser discharge nondimensionalized by  $F_x^o$  (the force in the  $x$ -direction before the laser is discharged) versus time. The forces are calculated over the entire hemisphere cylinder. The lower horizontal axis is the dimensionless time,  $tU_\infty/R$ , where  $R$  is the hemisphere radius. The upper horizontal axis is dimensional time in  $\mu\text{s}$  where  $t = 0$  s is the instant that the laser discharge is added to the flow. Dashed lines show the zero change in the force, i.e., in the  $x$ -direction, the total force is equal to the total drag force of the hemisphere-cylinder before laser discharge; and in the  $y$ -direction, the total force is equal to zero. The change in the  $x$ -direction force shows drag reduction while the change in the  $y$ -direction force can be used for calculating the pitching moment on the hemisphere-cylinder.

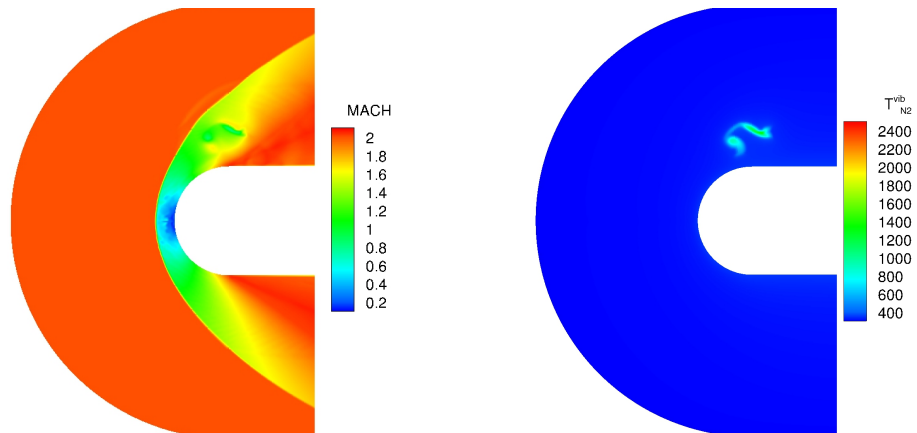
The first peak in the force change in the  $x$ -direction happens concurrent with the negative peak in the  $y$ -direction force and is due to the interaction of the shock wave with the hemisphere surface, which increases the pressure at the surface and hence the drag force. The creation of the vortex and its slow movement around the hemisphere surface is the reason for the long lasting drag reduction, which extends for about two dimensionless times. The dimensionless time of one is the time the freestream flow requires to pass a



(a)  $t = 14.45 \mu\text{s}$



(b)  $t = 43.35 \mu\text{s}$



(c)  $t = 120.41 \mu\text{s}$

Figure 7. Contour plots of Mach number and vibrational temperature of  $\text{N}_2$  for off-axis laser discharge.

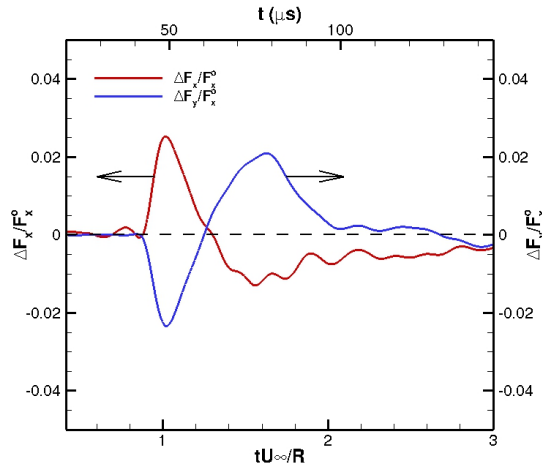


Figure 8. Dimensionless force change versus time for off-axis laser discharge.

distance equal to the hemisphere radius. The lower pressure at the center of the vortex causes a positive force in the  $y$ -direction along with the drag reduction. It should be noted that the maximum instantaneous change in the force in the  $y$ -direction is comparable to the maximum drag reduction.

## V. Conclusion

Simulations of laser discharge interaction with a 2.54 centimeter radius hemisphere cylinder at Mach 2 flow are performed. For the on-axis laser discharge, increasing the actual energy absorbed by the gas increased the gas dynamic energetic efficiency at the beginning until it reached its asymptotic value of about 3.0 at 25 mJ where increasing the actual energy absorbed by the gas up to 100 mJ has negligible effect on the gas dynamic energetic efficiency. The off-axis laser discharge reduces drag and also creates a side force. The maximum instantaneous change in side force is proportionate to the maximum drag reduction.

## References

- <sup>1</sup>Artem'ev, V., Bergel'son, V., Nemchinov, I., Orlova, T., Smirnov, A., and Khazins, V., "Change of Regime in Supersonic Flow Past on Obstacle Preceded by a Thin Channel of Reduced Density," *Izvestiya Akademii Nauk SSSR, Mekhanika Zhidkosti i Gaza*, Vol. 5, No. September-October, 1989, pp. 146–151.
- <sup>2</sup>Tretyakov, P., Garanin, A., Kraynev, V., Tupikin, A., and Yakovlev, V., "Investigation of Local Laser Energy Release Influence on Supersonic Flow by Methods of Aerophysical Experiments," *International Conference on Methods of Aerophysical Research, Novosibirsk, Russia*, 1996.
- <sup>3</sup>Riggins, D., Nelson, H., and Johnson, E., "Blunt-Body Wave Drag Reduction Using Focused Energy Deposition," *AIAA Journal*, Vol. 37, No. 4, 1999, pp. 460–467. doi:10.2514/2.756.
- <sup>4</sup>Lashkov, V., Mashek, I., Anisimov, Y., Ivanov, V., Kolesnichenko, Y., Ryvkin, M., and Gorynya, A., "Gas Dynamic Effect of Microwave Discharge on Supersonic Cone-shaped Bodies," AIAA Paper 2004-0671, American Institute of Aeronautics and Astronautics, January 2004. doi:10.2514/6.2004-671.
- <sup>5</sup>Adelgren, R., Yan, H., Elliott, G., Knight, D., Beutner, T., and Zheltovodov, A., "Control of Edney IV Interaction by Pulsed Laser Energy Deposition," *AIAA Journal*, Vol. 43, No. 2, 2005, pp. 256–269. doi:10.2514/1.7036.
- <sup>6</sup>Knight, D., Kolesnichenko, Y., Brovkin, V., Khmara, D., Lashkov, V., and Mashek, I., "Interaction of Microwave-Generated Plasma with a Hemisphere Cylinder at Mach 2.1," *AIAA Journal*, Vol. 47, No. 12, 2009, pp. 2996–3010. doi:10.2514/1.43657.
- <sup>7</sup>Schülein, E., Zheltovodov, A., Pimonov, E., and Loginov, M., "Experimental and Numerical Modeling of the Bow Shock Interaction with Pulse-Heated Air Bubbles," *International Journal of Aerospace Innovations*, Vol. 2, No. 3, 2010, pp. 165–188. doi:10.1260/1757-2258.2.3.165.
- <sup>8</sup>Kim, J., Matsuda, A., Sakai, T., and Sasoh, A., "Wave Drag Reduction with Acting Spike Induced by Laser-Pulse Energy Depositions," *AIAA Journal*, Vol. 49, No. 9, 2011, pp. 2076–2078. doi:10.2514/1.J051145.
- <sup>9</sup>Kremeyer, K., Sebastian, K., and Shu, C., "Computational Study of Shock Mitigation and Drag Reduction by Pulsed Energy Lines," *AIAA Journal*, Vol. 44, No. 8, 2006, pp. 1720–1731. doi:10.2514/1.17854.
- <sup>10</sup>Knight, D., "Survey of Aerodynamic Drag Reduction at High Speed by Energy Deposition," *Journal of Propulsion and Power*, Vol. 24, No. 6, November-December 2008, pp. 1153–1167. doi:10.2514/1.24595.

<sup>11</sup>Kianvashrad, N., Knight, D., Wilkinson, S., Chou, A., Horne, R., Herring, G., Beeler, G., and Jangda, M., “Effect of Off-Body Laser Discharge on Drag Reduction of Hemisphere Cylinder in Supersonic Flow,” AIAA Paper 2017-3478, American Institute of Aeronautics and Astronautics, June 2017.

<sup>12</sup>Dillon, J., Trimpi, R., and Schultz, A., “The NASA-Langley 20-Inch Supersonic Wind Tunnel,” AIAA Paper 86-0765, American Institute of Aeronautics and Astronautics, March 1986. doi:10.2514/6.1986-765.

<sup>13</sup>Park, C., “On Convergence of Computation of Chemically Reacting Flow,” AIAA Paper 1985-0247, American Institute of Aeronautics and Astronautics, January 1985. doi:10.2514/6.1985-247.

<sup>14</sup>Landau, L. and Teller, E., “Zur Theorie der Schalldispersion,” *Physikalische Zeitschrift der Sowjetunion*, Vol. 10, 1936, pp. 34–43.

<sup>15</sup>Kianvashrad, N. and Knight, D., “Simulation of Hypersonic Shock Wave Laminar Boundary Layer Interaction on Hollow Cylinder Flare,” AIAA Paper 2016-0349, American Institute of Aeronautics and Astronautics, January 2016. doi:10.2514/6.2016-0349.

<sup>16</sup>Roe, P., “Approximate Riemann Solvers, Parameter Vectors, and Difference Schemes,” *Journal of Computational Physics*, Vol. 43, No. 2, October 1981, pp. 357–372. doi:10.1016/0021-9991(81)90128-5.

<sup>17</sup>Knight, D., *Elements of Numerical Methods for Compressible Flows*, Cambridge University Press, New York, 2006.

<sup>18</sup>Wright, M., Bose, D., and Candler, G., “A Data-Parallel Line Relaxation Model for the Navier-Stokes Equations,” *AIAA Journal*, Vol. 36, No. 9, 1998, pp. 1603–1609. doi:10.2514/2.586.